SCIENCE CHINA
Chemistry

• ARTICLES •

August 2013 Vol.56 No.8: 1152–1163
doi: 10.1007/s11426-013-4849-1

High hydrosilylation efficiency of porous silicon SiH*x* species produced by Pt-assisted chemical etching for biochip fabrication

XIAO MinYu[1], HAN HuanMei[1,2] & XIAO ShouJun[1*]

[1]*State Key Laboratory of Coordination Chemistry, School of Chemistry and Chemical Engineering, Nanjing National Laboratory of Microstructures, Nanjing University, Nanjing 210093, China*
[2]*Jinan Entry-Exit Inspection and Quarantine Bureau Inspection, Jinan 250014, China*

Received December 22, 2012; accepted January 30, 2013; published online February 22, 2013

Porous silicon (PSi) prepared from Pt metal-assisted chemical etching (MaCE) was demonstrated to possess higher hydrosilylation efficiency (~57%) than anodized PSi (~11%) by surface reaction with ω-undecenyl alcohol (UO). Deconvolution of the SiH*x* (*x* = 1–3) stretching bands revealed the abundance of SiH_2 species on MaCE PSi was 53%, ~10% higher than on anodized samples, while both of SiH_1 and SiH_3 were ~5% lower correspondently on MaCE PSi than on anodized samples. The surface SiH*x* abundances were suggested to account for the higher hydrosilylation efficiency on MaCE PSi. Optimization of Pt-assisted chemical etching parameters suggested a 7–15 nm thick Pt-coating and an etching time of 3–10 min for biochip applications. Scanning electron microscopy images revealed that an isotropic top meso-porous layer was beneficial for hydrosilylation and long-term durability under ambient conditions. To end, an example of histidine-tagged protein immobilization and microarray was illustrated. Combining the materials' property, surface chemistry, and micro-fabrication technology together, we envision that silicon based biochip applications have a prosperous future.

metal-assisted chemical etching, porous silicon, surface chemistry, hydrosilylation, biochip

1 Introduction

The strategy of organic functionalization of porous silicon (PSi) has been widely used for many applications such as silicon photonics, biosensing, and solar cells [1–5]. Hydrosilylation between vinyl groups of organic molecules and PSi surface SiH*x* species is the well-known organic functionalization approach [6, 7]. PSi is conventionally fabricated by anodic (electrochemical) etching using hydrofluoric acid (HF)-based ethanolic solution, thus organic modification is mainly applied to the anodized PSi. However, a still remaining challenge on the application of anodized PSi, even after surface modification, is degradation in aqueous media, organic solvents, and ambient atmosphere. Depending on the immobilized molecules and ambient environmental conditions, the loss of the porous membrane often occurs in hours to days, mainly due to the nanometer scale pores and columns [8–10]. Recently, an alternative way to prepare more robust PSi by metal-assisted chemical etching (MaCE) [11] is attracting more and more attention for its easy and economic aspects. In the MaCE approach, a thin metallic film (Au, Pt, Al, Pd, etc.) is deposited directly on a silicon surface prior to immersion in a chemical stain etchant composed of HF-based ethanolic solution and an oxidizing agent such as hydrogen peroxide (H_2O_2), nitric acid (HNO_3) or sodium persulphate ($Na_2S_2O_8$) [11–13]. The thin metallic film facilitates the stain chemical etching on silicon and thus a porous silicon layer can be formed in a short time (seconds to minutes), much faster than the stain chemical etching applied on a silicon chip which needs hours to days. Bohn *et al*. [11], pioneers of the MaCE approach, proposed a mechanism in a 1:1:1 (*v*/*v*/*v*) HF(49%):H_2O_2(30%):EtOH

*Corresponding author (email: sjxiao@nju.edu.cn)

etching solution that the ultrathin metal film acted as a local cathode to mediate the reduction of H_2O_2 and consequently the hole injection occurred in silicon to accelerate the formation of porous structures. They mentioned that the passivation layer of SiO_2 had little effect on preparing porous structures, especially on the porous morphologies [11–13]. However, the content of surface SiH*x* species prepared in the MaCE system without moving the passivation layer (SiO_2) away is much lower (5–10 times less) than in the anodized samples within an etching time window of around 1–10 min, in order to prepare a relatively flat, thin and porous membrane for biochip applications. A low surface SiH*x* concentration will generate a loose organic monolayer via hydrosilylation rather than a densely covered monolayer. The partial surface coverage will bring further oxidation of silicon, triggered from exposed metallic silicon sites, and finally will result in degradation of the porous structure, especially in aqueous media or under ambient atmosphere. In contrast, the fully covered organic monolayers and, especially, polymer brushes provide better protection for the porous structure and improve its durability under ambient conditions [8–10]. Incidentally, we found that the surface SiH*x* species could be enhanced greatly in the MaCE system by removing the passivation SiO_2 layer first and then depositing the Pt film. This approach increased the SiH*x* species to about 5–10 times as on the passivation SiO_2 layer covered silicon chip in the MaCE system, reaching the same level as on the anodized samples. We have endeavored to fabricate organic functionalized PSi matrices for biomedical applications [14–20]. Recently we applied the MaCE PSi as supporting substrate for hydrosilylation and further for fabrication of long-term durable biochips which lasted for weeks to months, mainly due to the mesostructure and mesometer scale pores and columns [11, 17]. We observed that the SiH*x* (x = 1–3) species were converted more easily and neatly to organic monolayers by hydrosilylation with vinyl groups of organic molecules in MaCE PSi than in anodized PSi. This qualitative observation was illustrated with infrared absorption spectra, where after hydrosilylation the remaining SiH*x* and the back-side oxidized (O)SiH*x* stretching bands at around 2110 cm^{-1}, and especially the Si–O stretching bands at around 1100 cm^{-1} from side products of SiO_2 and Si–OR were attenuated greatly [17].

Because MaCE PSi possesses the advantages of both the long-term durable porous structure under ambient conditions and the high hydrosilylation efficiency, compared to anodized PSi, it is obviously beneficial for biosensing applications. To explore the details of the different hydrosilylation mechanisms between MaCE PSi and anodized PSi, we easily observed the different band shapes in the multiple SiH*x* stretching region, indicating the different abundances of SiH_1, SiH_2 and SiH_3 species respectively. Since all other reaction parameters during hydrosilylation were the same, it was rational to refer that SiH_1, SiH_2 and SiH_3 species possessed different hydrosilylation reactivities. We first fitted the SiH*x* bands with three SiH_1, SiH_2 and SiH_3 species on both MaCE and anodized PSi samples, analyzed their compositions, and proposed the different hydrosilylation mechanisms with the radical reactivity theory. Then we optimized the etching parameters to generate suitable surface SiH*x* species and topographies for fabrication of biochips: (1) an optimum etchant with fixed volume ratios of 2:2:1 (*v*:*v*:*v*) HF(40%):H_2O_2(30%):EtOH was adopted from our previous report [20], (2) Pt-coatings were assessed with infrared spectroscopy to be in the thickness of 7–15 nm, (3) the etching time was evaluated with infrared spectroscopy and scanning electron microscopy (SEM) to be between 3 and 10 min.

Further we provided infrared experimental data to estimate the surface hydrosilylation efficiency with ω-undecenyl alcohol (UO) on both MaCE and anodized PSi. The target reaction yields were estimated on MaCE PSi as ~57%, while only ~11% on anodized PSi, by means of the integrated absorbance ratio of –OH stretching band over per alkyl CH_2 stretching bands. The phenomena were explained as, for bi-functional molecules such as UO and ω-undecenyl acid, besides hydrosilylation reactions, side reactions between surface SiH*x* species and hydroxyl (–OH) or carboxyl (–COOH) groups occurred [21–26]. It is the side reactions that affect greatly the target hydrosilylation reaction. Since the end functional hydroxyl or carboxyl groups are often required for further surface functionalizations such as growing polymer brushes and attaching biomolecules, surface SiH*x* hydrosilylation efficiencies, especially with both end-functionalized molecules such as UO and ω-undecenyl acid, need to be enhanced.

To end, we showed an application example to successfully fabricate a protein microarray on the MaCE PSi substrate, combining surface chemistry and photolithography. While with anodized PSi as the substrate we failed to do so because of the degradation and loss of the vulnerable porous layer. Briefly, the end hydroxyl groups of UO was converted to a surface initiator, poly(acrylic acid) (PAA) brushes were grown by atom transfer radical polymerization (ATRP) [18, 19], PAA microarray patterns were generated by photolithography and the exposed PAA patterns were derivatized into NTA(nitrilotriacetic acid)-Ni^{2+} micro-spots, finally histidine-tagged proteins were captured on the NTA-Ni^{2+} spots by affinity binding for microarray demonstration [15–17].

This paper is a continuation of our on-going exploration of MaCE PSi as a long-term durable supporting substrate for surface modification and further for biosensing [17–19]. Our findings are: (1) the content of surface SiH*x* species dramatically increased in MaCE under optimized etching conditions by removing the passivation SiO_2 layer from silicon surface, followed with deposition of a nanometer scale Pt film; (2) the different SiH*x* stretching band shapes

between MaCE PSi and anodized PSi were distinguished by deconvolution and a higher content of SiH_2 species and lower contents of SiH_1 and SiH_3 in MaCE PSi than in anodized PSi respectively were proposed to be responsible for the higher hydrosilylation efficiency of MaCE PSi; (3) the surface hydrosilylation efficiency was estimated on UO-grafted MaCE and anodized PSi by means of the integrated absorbance ratios of –OH stretching band over per alkyl $–CH_2$ stretching bands; (4) a long-term durable PSi protein chip was exemplified by stepwise surface reactions to grow poly(acrylic acid) brushes and fabricate NTA-Ni^{2+}/histidine-tagged protein microarrays.

2 Experimental methods

2.1 Materials

Single-side polished silicon wafers (<100>, p-type, boron-doped, 5.0–8.0 Ω cm, 500 μm thick) were purchased from Hefei Kejing Materials Technology CO. LTD. *N*-Ethyl-*N*′-(3-(dimethylamino)propyl)carbodiimide hydrochloride (EDC) (98%), ω-undecanol (⩾ 99.5%, GC grade) and ω-undecenyl alcohol (UO) (⩾ 98%, GC grade) were from Aladdin. N-Hydroxysuccinimide (NHS) (98%), bipyridine, tert-butyl acrylate, 2-bromoisobutyryl bromide (98%), and 4-morpholineethanesulfonic acid hydrate (MES) were from Alfa Aesar. Copper (I) bromide (CuBr, 98%) was from Aldrich. *N*α,*N*α-Bis(carboxymethyl)-L-lysine hydrate (abbreviated as ANTA) was from Fluka. FITC (fluorescein isothiocyanate)-labeled histidine-tagged thioredoxin-urodilatin (abbreviated as FITC-labeled His-tagged Trx-urodilatin) was prepared according to our previous report [15, 16]. All the other reagents are analytical grade except being mentioned specially. Water (18 MΩ cm) was from a Milli-Q ultrapure water purification system.

2.2 Metal-assisted chemical etching to prepare PSi

Single side polished <100> oriented p-type silicon wafers were boiled in 3:1 (*v*/*v*) concentrated H_2SO_4/30% H_2O_2 for 30 min and then rinsed copiously with water and ethanol. The cleaned wafers were stored in water at room temperature before being used. After the passivation silica layer from a silicon chip (2×2 cm) was removed with 2 min dip in 2% HF solution, a thin metallic film of Pt was deposited on the polished side of the chip with a sputter coater (SCD 500). Different thicknesses of Pt-coatings (2.8, 5.2, 7.8, 10.2, 12.8, 15.6 nm) were obtained by sputtering at 15 mA for 40, 80, 120, 160, 200, and 240 seconds. The thin Pt-film coated silicon chip was etched in an optimized etchant, composed of 2:2:1 (*v*:*v*:*v*) 40%HF:30%H_2O_2:EtOH for seconds to minutes in dark [20]. A cross-checking approach was applied to optimize the etching parameters of thickness of Pt-coatings and etching time. First, the optimum thickness of Pt-coatings was analyzed with the infrared spectra by fixing the etching time to 4 min. The optimum etching time was assessed with infrared spectroscopy and scanning electron microscopy (SEM, Hitachi S-4800 at an accelerating voltage of 15.0 kV) by fixing the thickness of Pt-coating to 12.8 nm. The MaCE PSi chips prepared with etching parameters of 12.8 nm Pt-coatings and 4 min etching were used for further organic modifications. Anodized PSi for control experiments was prepared in a 1:3 (*v*:*v*) solution of pure ethanol and 40% aqueous HF for 8 min at a current density of 60 mA/cm^2 [14]. The freshly etched chips were cleaned as follows: rinsed with copious amounts of ethanol and dried with a stream of N_2. They were used for further organic modifications immediately or stored in a desiccator, which should be used within a day.

2.3 Surface hydrosilylation, end group conversion, and atom transfer radical polymerization (ATRP) for polymer brushes

A freshly etched silicon chip was transferred into a vial (80 mL) containing 10 mL neat UO. The bottle was purged with pure nitrogen for 30 min so as to vent the air. The reaction was performed in a CEM Discovery microwave reactor, controlled with a dynamic mode to reach 120 ºC in 10 min and held there for 20 min. After reaction, the chip was washed sonically with anhydrous alcohol for 3 min and dried with N_2. The UO-reacted chip was assayed with infrared spectrometer to estimate the hydrosilylation reaction yield.

To use such a PSi chip as substrate for microarray fabrication, we further grew polymer brushes, generated microarray patterns by micro-fabrication technology, and captured fluorescence-labeled proteins in patterns for imaging. Since we described the details of growing poly(acrylic acid) (PAA) and poly(methacrylic acid) (PMAA) brushes and their different EDC/NHS activation mechanisms in a recent report [18], where PAA was illustrated to have higher biomolecular loading efficiency, we selected PAA brushes to fabricate protein microarrays. The UO-modified chip with hydroxy-termini was put into a glass bottle containing 10 mL CH_2Cl_2 and 0.1 g 4-dimethylamiopryidine; the reaction vessel was cooled in an ice bath for 15 min; then 2-bromoisobutyryl bromide (2 mL) was dropped in slowly, stirred at 0 °C for 2 h, and stayed at room temperature for another 10 h. Rinsed with copious CH_2Cl_2 and ethanol to remove the excess of unreacted and physico-adsorbed reagents, and dried, the PSi chip was terminated with a surface initiator of 2-bromoisobutyryl group. To increase the surface loading capability of biomolecules, poly(tert-butyl acrylate) brushes were grown by immersing the chip in a N_2-filled Schlenk flask with a 3 mL solution of monomer (tert-butyl acrylate)/CH_3OH (1/2 in *v*/*v*) containing 18 mg (0.125 mmol) CuBr and 40 mg (0.26 mmol) bipyridine at 40 °C for 8 h. Then, the chip was removed from the solution,

washed with THF and ethanol sequentially, and dried. PAA brushes were obtained by hydrolysis of poly(tert-butyl acrylate) in a solution of methanesulfonic acid (0.3 mL) in dichloromethane (10 mL) for 3 h at room temperature. The thickness of PAA brushes after staining with 1% acetate uranium for 5 min was measured to be at around 150 nm by SEM cross section imaging.

2.4 Fabrication of protein microarray

The microarray patterns were fabricated on the PAA brushes coated PSi chip by photolithography in clean room. First PAA covered PSi chips were blown dry with mild nitrogen stream and placed on a heating plate at 100 °C for 5 min to evaporate moisture completely. An AZ2700 positive photoresist was spin-coated onto the PSi chip at 600 rpm for 5 seconds and then at 3000 rpm for 30 seconds, then soft-baked at 100 °C for 5 min. A photomask pattern was transferred onto the substrate by exposure to UV (λ = 360 nm, 100 mJ/cm^2) irradiation. The photo-exposed chip was immersed in a ZX-238 developing solution for 15 seconds, washed with copious water and hard-baked at 100 °C for 15 min to generate micro-spot arrays surrounded with photoresists. The diameter of spots was 200 μm and the neighbor spot-spot distance was 600 μm.

The exposed PAA patterns were activated to NHS esters by immersion in a solution of NHS (0.092 g, 0.8 mmol) and EDC (0.076 g, 0.4 mmol) in 4 mL MES buffer (0.1 M, pH 6.0) at room temperature for 1 h, then the chip was washed with water and dried with nitrogen. Next, the chip was incubated in 3 mL ANTA solution (100 mM ANTA in a K_2CO_3 solution, pH 8.0) for 40 min to obtain the nitrilotriacetic acid (NTA) microarrays. Rinsed with water, the chip was incubated in 5 mL $NiSO_4$ solution (100 mM/L) for 40 min at room temperature to load Ni^{2+}. Rinsed with water and dried, the chip was washed with acetone to remove the rest of photoresists. Finally, the protein of FITC-labeled His-tagged Trx-urodilatin (0.2 mg/mL, 10 μM) in 20 mM Tris-HCl buffer (0.1 M NaCl and pH 7.9) was captured by NTA-Ni^{2+} after 1 h incubation [15, 16].

Fluorescence imaging was carried out on a Tecan LS300 Scanner at a photomultiplier tube (PMT) gain of 150. The excitation was with an argon ion laser at 488 nm, and the fluorescent emission signal was gained using a 535 nm wavelength filter.

2.5 Transmission FTIR measurements

Transmission Fourier-transform (FTIR) infrared spectra were recorded with a Bruker V80 spectrometer at 4 cm^{-1} resolution. Typically 32 scans were acquired per spectrum. A planar untreated Si <100> wafer was used as a reference. The absorbance mode of IR spectra was used to quantify the surface concentration of grafted molecules. All spectra were recorded using non-patterned porous silicon chips.

3 Results and discussion

3.1 Comparison of SiH*x* composition on MaCE and anodized PSi samples

In our previous report [17], we found that surface hydrosilylation was more efficient on PSi prepared by Pt-assisted chemical etching than by electrochemical etching, judged mainly from the FTIR spectra qualitatively. Although the silicon surface hydrosilylation chemistry has been carefully investigated on anodized porous silicon and single crystalline silicon [6, 7, 27–37], comparing the hydrosilylation reaction performance and mechanisms between different substrates is rare. Here by fitting and analyzing the SiH*x* spectra quantitatively, we tried to explore and understand the different surface hydrosilylation mechanisms. Firstly, we illustrated two infrared spectral traces of freshly etched PSi samples in Figure 1, where trace (a) was from anodization and (b) from MaCE. It is well accepted that all bands in Figure 1 are from different vibration modes of SiH*x* species: multiple SiH*x* stretching bands in the region of 2050–2200 cm^{-1}, and SiH*x* scissoring, bending, and wagging bands in the fingerprint region of 500–1000 cm^{-1} [38–40]. The feature bands on both traces (a) and (b) appear similar in shape, however the band intensities are much different, especially for the SiH_1, SiH_2, and SiH_3 stretching, bending and scissoring strengths. We rationalized that monohydride (SiH_1), dihydride (SiH_2), and trihydride (SiH_3) possessed different reactivities toward hydrosilylation, therefore different abundances (or compositions) of SiH*x* species should be the main parameters to be dealt with. Since the stretching bands of SiH*x* from PSi have multiple peaks and they overlap with each other, the exact assignments are difficult, and still in debate [38–40]. For example, the assignments of

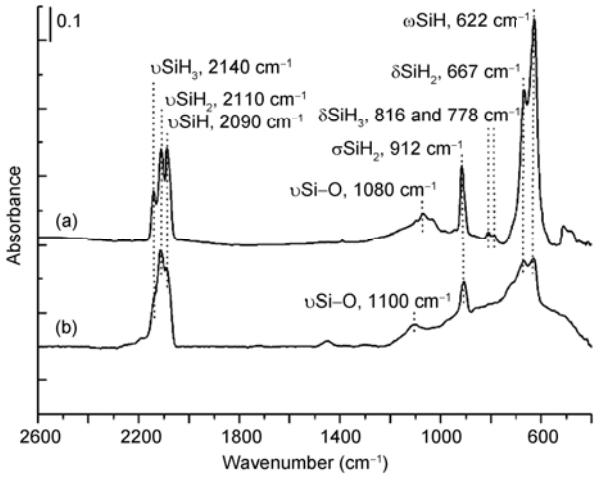

Figure 1 Transmission FTIR of freshly etched PSi prepared by (a) electrochemical etching in a 1:3 (*v*:*v*) solution of pure ethanol and 40% aqueous HF for 8 min at a current density of 60 mA/cm^2 and (b) Pt-coating (12.8 nm thick) assisted chemical etching in a 2:2:1 (*v*:*v*:*v*) solution of 40%HF:30%H_2O_2:EtOH for 4 min. Abbreviations: υ, stretching; δ, bending; ω, wagging; σ, scissoring.

SiH*x* symmetric and asymmetric stretching bands cannot be pinned down because they cannot be well resolved and distinguished, not like the CH*x* symmetric and asymmetric stretching bands separated distinctly. We adapted the mostly accepted concept of three stretching bands: SiH_1 at ~2090, SiH_2 at ~2010, and SiH_3 at ~2140 cm^{-1}. However an obvious shoulder at ~2075 cm^{-1} appeared beside the main SiH_1 peak of 2090 cm^{-1} in the SiH*x* stretching region, both for anodized and MaCE PSi (Figure 2), which had to be fitted with one more peak. The two SiH_1 fitting bands could be explained as the isolated monohydride at 2075 cm^{-1} and clustered monohydride at 2090 cm^{-1}. We noticed that all four resolved bands on MaCE exhibited 4–6 cm^{-1} blue shift from those on anodized PSi. For example, SiH_2 on MaCE PSi is at 2116 cm^{-1}, 6 cm^{-1} higher than on anodized PSi at 2109 cm^{-1}. We suggest that the bond configurations and clusters, especially the hydride connected metallic Si-Si bond configurations, are responsible to the band shift [38–40].

The quantitative fitting results are shown in Figure 2. For anodized PSi in Figure 2(a), the integrated absorbance percentages are (24.17+15.98=) 40.15% SiH_1, 42.99% SiH_2, and 16.85% SiH_3 respectively, while for MaCE PSi in Figure 2(b), they are (23.68+10.50=) 34.18% SiH_1, 53.26% SiH_2, and 12.55% SiH_3 respectively. The infrared absorption coefficients of 3 silicon hydride species (SiH_1, SiH_2, and SiH_3) in hydrogenated amorphous silicon had been investigated intensively and were treated nearly equal to each other for quantitative analyses [38, 39]. Assuming that the SiH*x* absorption coefficients in our MaCE and anodized PSi samples obey the same rule, the integrated absorbance percentages of SiH_1, SiH_2 and SiH_3 represent their surface compositions respectively. Obviously, SiH_2 is ~10% higher, but both of SiH_1 and SiH_3 are ~5% lower correspondently in MaCE PSi than in anodized PSi.

The different surface SiH*x* abundances are proposed to account for the different hydrosilylation mechanisms. The radical generation of SiH*x* species triggered by light, heat, or microwave irradiation and then the radical abstraction by vinyl groups have been widely accepted for silicon surface hydrosilylation [6, 7, 27–37]. We apply the analogical reasoning for SiH*x* species to CH*x* species, to which the radical reactivity sequence is $\equiv C\cdot > =CH\cdot > -CH_2\cdot$; therefore the reactivity of radical species formed by SiH*x* will be $Si\cdot > SiH\cdot > SiH_2\cdot$, or in the reverse direction, the stability sequence is $Si\cdot < SiH\cdot < SiH_2\cdot$. Since MaCE PSi has higher hydrosilylation efficiency, we suggest that the best radical species for surface hydrosilylation is $SiH\cdot$ from SiH_2, the most reactive intermediate $Si\cdot$ species from SiH_1 is most easily to be quenched by oxygen species, for example, O_2 from air, –OH or –COOH from organic compounds, and the lowest reactive $SiH_2\cdot$ species from SiH_3 has much lower hydrosilylation efficiency. Since MaCE PSi contains 53% SiH_2, 10% more than anodized PSi (43% SiH_2), MaCE PSi definitely has higher hydrosilylation efficiency than anodized PSi according to the above hypothesis. In addition, the different SiH*x* configurations on MaCE PSi from anodized PSi may also account for their different hydrosilylation reactions.

In the fingerprint region from 1000 to 500 cm^{-1}, the well-resolved bands include the SiH_2 scissoring (912 cm^{-1}) and bending (667 cm^{-1}) modes and SiH_1 wagging (622 cm^{-1}) mode [38, 39]. The much higher intensities of both SiH_2 bending and SiH_1 wagging bands on anodized PSi, should relate to the orientation of silicon nanowires and nanopores, which were perpendicular to the substrate surface [14]. While for MaCE PSi, the SiH*x* scissoring, bending and wagging bands in this region exhibit medium strength, which should account for the outmost amorphous porous structures. The different etching parameters such as anodization or MaCE, solution, and etching rate manipulate the porous membrane nanostructure of morphologies, facets, SiH*x* configurations, and surface composition, and thus result in different surface hydrosilylation levels.

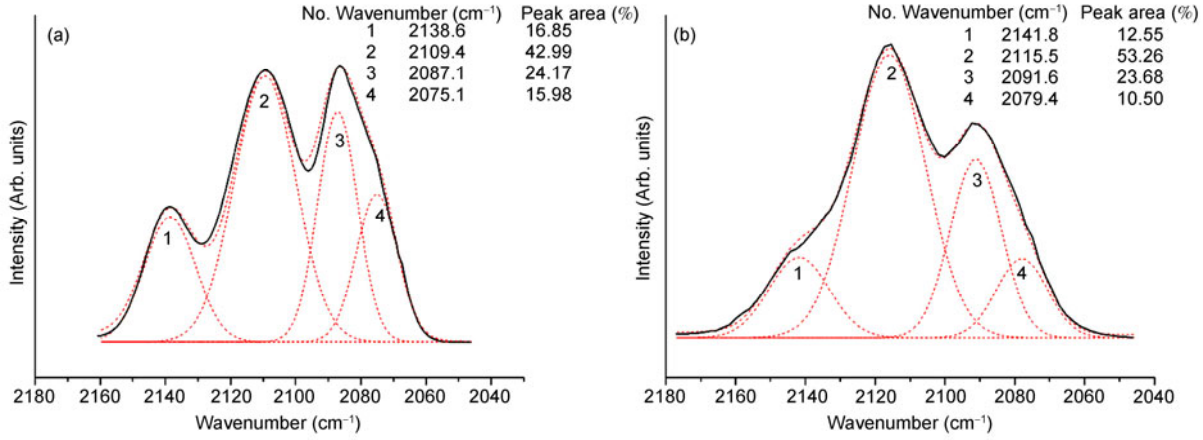

Figure 2 Deconvolution of SiH*x* stretching bands of anodized PSi (a) and MaCE PSi (b).

3.2 Optimization of etching conditions

To generate more SiH*x* species while maintain a relatively flat porous layer for biochip applications, optimization of the etching conditions is necessary. We investigated two parameters: Pt film thickness and etching time. An optimum etching solution composition was fixed to $V_{40\%HF}$:$V_{30\%H_2O_2}$:$V_{ethanol}$ = 2:2:1 according to our previous report [20].

3.2.1 Optimization of thickness of Pt-coatings for higher SiHx content

Figure 3 illustrates stacked SiH*x* stretching bands (a) and the integrated absorbance against the thickness of Pt-coatings (b). Obviously the curve in Figure 3(b) represents the quantity evolution of the whole SiH*x* species against the thickness of Pt-coatings. When the thickness was 2.8 or 5.2 nm, the amount of SiH*x* species was low, most probably due to the partial coverage of the thin Pt-coating and fast consuming-up of Pt metals during the early etching stage, resulting in slow etching and inhomogeneous surface structures. The most amount of SiH*x* species was obtained with a 10.2 nm Pt-coating. When the coating was thicker than 10.2 nm, the surface SiH*x* species began to decrease, which can be explained as the etching blocking effect from the thicker Pt-coating. The suitable amount of SiH*x* species for hydrosilylation, from our experience, was above an infrared absorbance of 0.2 at 2110 cm^{-1} (or an integrated absorbance of 15 for the whole SiH*x* stretching band), corresponding to Pt-coatings with a thickness from 7 to 15 nm.

3.2.2 Optimization of etching time for SiHx species

Figure 4(a) shows stacked SiH*x* stretching bands of a PSi chip with a 12.8 nm Pt-coating for different etching time and Figure 4(b) plots the integrated absorbance against the etching time. Figure 4(b) includes four curves, the integrated absorbance of the whole SiH*x* stretching bands (SiH_1+SiH_2+SiH_3) and three resolved respective integrated absorbance of SiH_1, SiH_2 and SiH_3 as well against the etching time. Since all the SiH*x* band shapes are similar, three resolved SiH_1, SiH_2 and SiH_3 bands in each trace present

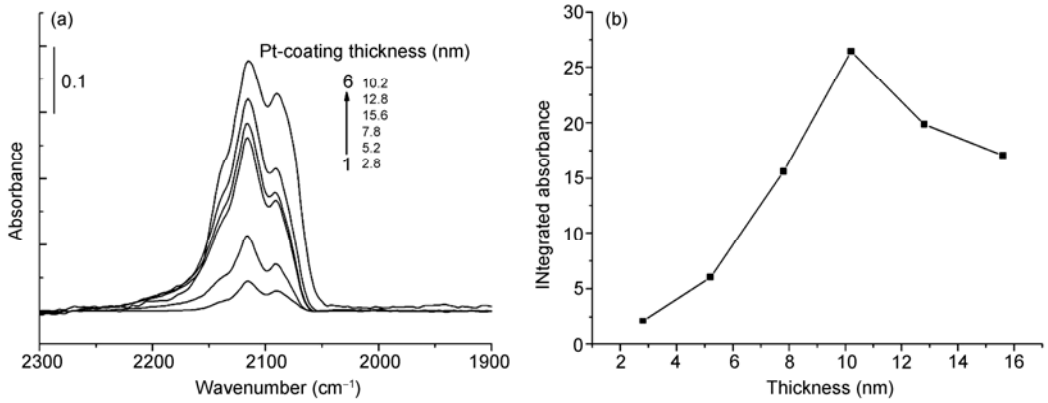

Figure 3 Influence of the thickness of Pt-coatings on SiH*x* with a fixed etching time of 4 min: (a) stacked SiH*x* stretching bands for different Pt-coatings with a thickness from bottom to top: (1) 2.8 nm, (2) 5.2 nm, (3) 7.8 nm, (4) 15.6 nm, (5) 12.8 nm, (6) 10.2 nm; (b) integrated absorbance from 2000 to 2250 cm^{-1} against the thickness of Pt-coatings.

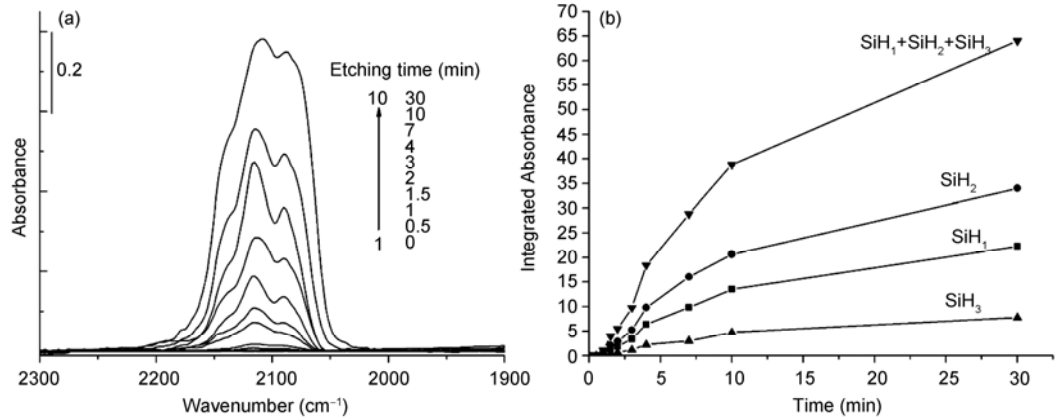

Figure 4 Influence of the etching time on SiH*x* with a fixed thickness of a 12.8 nm Pt-coating in a 2:2:1 (v:v:v) 40%HF:30%H_2O_2:EtOH etching solution: (a) stacked SiH*x* stretching bands for different etching time of 0, 0.5, 1, 1.5, 2, 3, 4, 7, 10 and 30 min, represented by traces of 1 to 10 from bottom to top respectively; (b) integrated absorbance from 2000 to 2250 cm^{-1} (SiH_1+SiH_2+SiH_3) and resolved respective integrated absorbance of SiH_1, SiH_2, and SiH_3 against the etching time.

nearly the same integrated absorbance ratios. At the early etching stage within 1 min, SiH*x* increased slowly because the etchant just started to etch Pt-coatings and had not yet immersed the silicon substrate completely. After the redox reaction was triggered, SiH*x* increased exponentially due to the accelerated reaction at the interface of Pt/Si up to 10 min. After 10 min, the Pt-coatings were nearly consumed up, and only the chemical etching played a role, thus the etching speed for producing SiH*x* species was attenuated. All the stacked traces in Figure 4(a) exhibit similar shapes, indicating the similar abundances of SiH_1, SiH_2 and SiH_3 species in the whole etching process. With the aforementioned absorbance of SiH*x* at 2110 cm^{-1} above 0.2 as a marker for effective hydrosilylation, the optimum etching time window was from 3 to 10 min.

3.2.3 Optimization of etching time for porous structures by SEM

The topomorphologies of MaCE PSi had been reported to be less homogeneous than those of anodized Psi [11–14, 17], where the meso-pores and meso-columns of MaCE PSi were in micro- and submicro-meter scale, while those of anodized PSi in tens of nanometer scale. For biochip applications, a relatively homogeneous surface is needed to attenuate the light scattering and to provide a low fluorescence background. Figure 5 illustrates the evolution of porous structures against the etching time with SEM images, both by topomorphology and cross section profile. Before etching (0 min), both images showed a flat, homogenous, and dense Pt-coating (12.8 nm) on the SiO_2-free silicon chip. After 0.5 min etching, 2–4 μm pores were formed on the Pt-coating, due to the erosion of platinum from the most vigorous redox reaction sites at the Pt/Si interface; while from the cross section profile, a ~10 nm thick Pt-coating was followed with a ~50 nm porous silicon layer. After 1.5 min etching, more and smaller pores with 1–2 μm diameter were observed, which were real pores formed on the silicon surface; Pt-coatings in the pore area sunk into the bottom while those atop the wall area still stayed on the top; from the cross section profile, an ultrathin Pt-sheet (~2 nm thick) was observed to cover the silicon surface, and a 200–300 nm porous silicon layer was clearly under the Pt-sheet. After 4 min etching, the topomorphological pores kept the similar size of 1–2 μm diameter, but looked shallow and flattened, due to the attenuated imaging contrast between the wall and the pore, where both were silicon materials. While for the topomorphology images at 0.5 and 1.5 min, the pores, looking much deeper, were brought to us by the high electron scattering contrast in SEM between Pt-coating sheets on the top and silicon in the pores. The cross section image at 4 min showed an amorphous sponge-like structure layer on the top and a few deep pores with nanometer diameter into the silicon body (~5 μm deep). After 10 min etching, the topomorphology showed larger surface pores (2–3 μm in diameter), while the cross section profile illustrated much denser pores with submicrometer diameter extended deeply into the silicon body up to 10 μm. From the cross section profiles of 1.5, 4, and 10 min, two layers of porous structures can be classified: the first outmost layer, hundreds of nanometers thick, generated underneath the Pt-coating, was meso-porous and isotropic in pore orientations; the second layer was an anisotropic porous structure with vertical nano- to micro-meter diameter pores extending 1–10 μm deep into the silicon body.

To summarize from the above analyses, the protocol for producing MaCE PSi to meet biochip applications is: (1) remove the passivation layer of SiO_2 from silicon chips with a dilute HF solution (1%–2%), (2) sputter Pt-coatings on silicon with a thickness of 7–15 nm, (3) etch in an etchant solution with volume fractions of 40% HF in 30%–65%, 30% H_2O_2 in 40%–55%, and ethanol in 15%–40% [20], (4) etch for 3–10 min.

3.3 Hydrosilylation efficiency between SiH*x* and UO

To quantitatively compare the hydrosilylation reaction efficiency between the MaCE and anodized PSi samples, we analyzed an example reaction, grafting UO on freshly etched PSi samples. UO is the mostly used reagent in surface hydrosilylation for further growing polymer brushes and fabricating biochips [18, 19, 37]. It contains both end vinyl and hydroxyl groups, which have been reported to react with SiH*x* species simultaneously. For fabrication of biochips, high surface hydrosilylation efficiency is needed to increase the concentration of hydroxyl groups, i.e. most of SiH*x* species react with vinyl groups, while the side reaction of SiH*x* + HO–R = Si–OR and oxidization of SiH*x* to SiO_2 should be attenuated. Using the microwave irradiation, we found obvious intensity differences of the hydroxyl stretching bands at ~3340 cm^{-1} between MaCE PSi in Figure 6(c) and anodized PSi in Figure 6(d). To evidence the covalent grafting of UO on PSi and to estimate the hydrosilylation efficiency, we showed the IR spectra of pure UO and undecanol films casted on silicon in Figures 6(a) and (b) respectively. The covalent grafting of UO was evidenced by the disappearance of the stretching bands of vinyl groups at 3078 (vinyl C–H asymmetric stretching), 2979 (vinyl C–H symmetric stretching), 1643 (C=C stretching), and 910 (vinyl C–H bending) cm^{-1} in Figures 6(c) and (d). The oxidation band of Si-O centered at 1100 cm^{-1} is quite strong in anodized PSi (Figure 6(d)), attributed by side products of both SiO_2 and Si–O–C [14]; while it is much smaller in MaCE PSi (Figure 6(c)) due to the higher hydrosilylation effect, in accordance to our previous report [17]; it is also slightly visible in neat UO and undecanol casted samples (Figures 6(a, b)), owing to the imbalance of the passivation layer of SiO_2 between samples and the reference.

We designed a strategy as follows to estimate the hy-

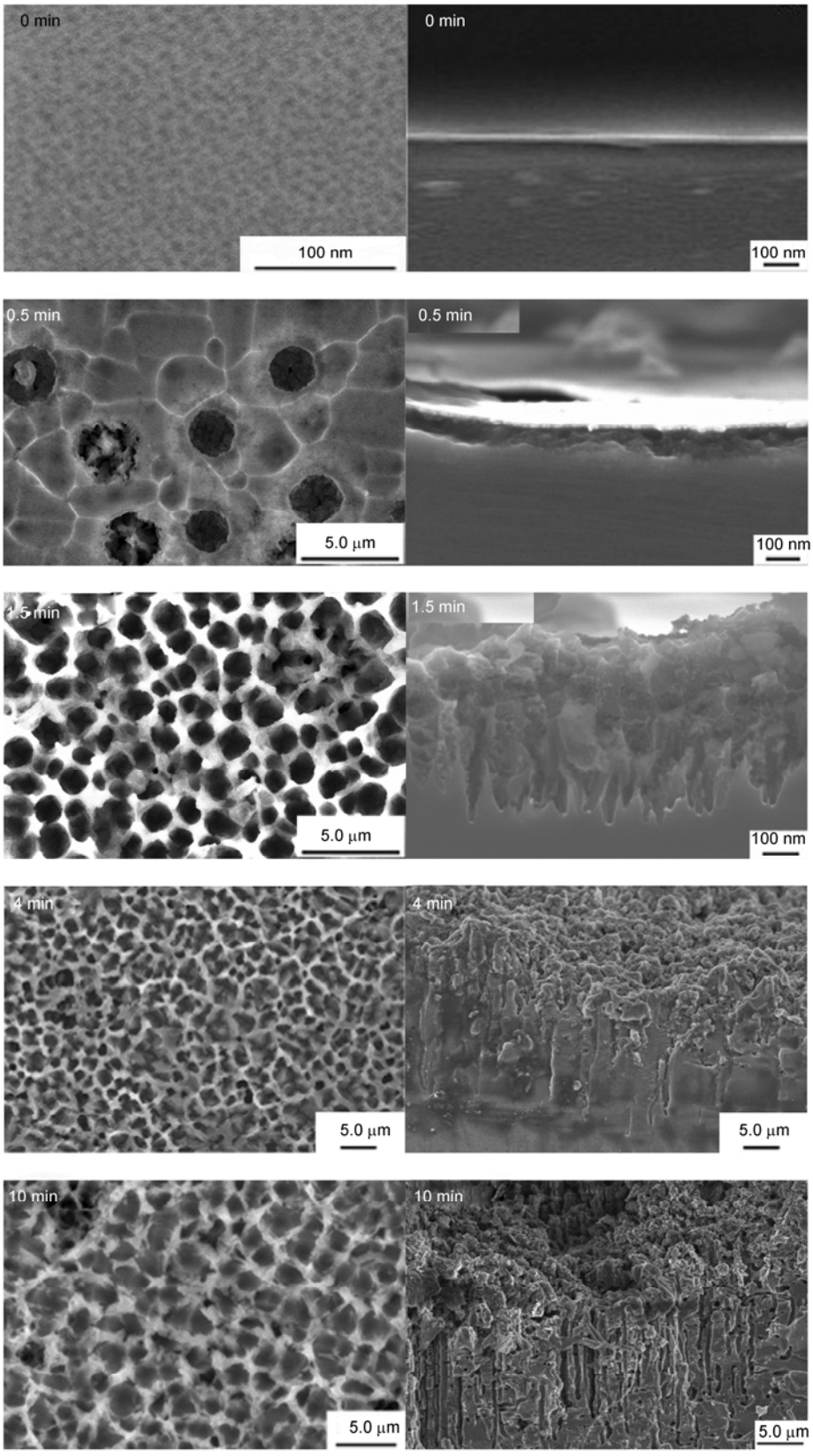

Figure 5 Evolution of topomorphology (left) and cross section profile (right) of the porous silicon layer against the etching time.

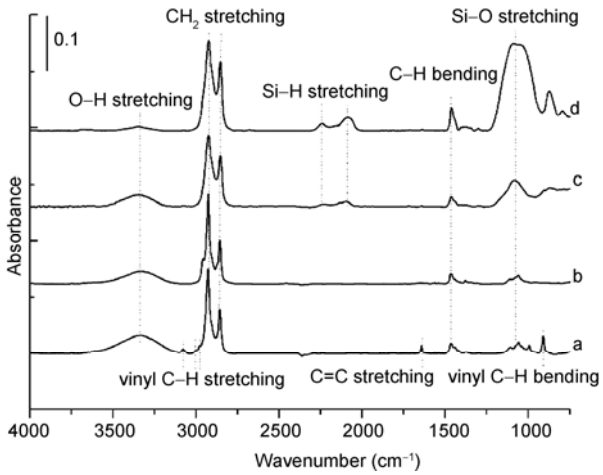

Figure 6 Transmission infrared spectra of (a) pure UO film casted on a silicon chip, (b) pure undecanol film casted on a silicon chip, (c) grafted UO on MaCE PSi, and (d) grafted UO on anodized PSi.

drosilylation efficiency: first the C–H and O–H stretching bands in the region from 2700 to 3700 cm^{-1} for all four traces in Figure 6 were fitted and the abundance of each peak was obtained (see Figure S1 in Supporting Information); then the ratio of $r = A_{OHs}/A_{CH_2s}$ was calculated, where A_{OHs} represents the integrated absorbance of O–H stretching band centered at 3340 cm^{-1}, and A_{CH_2s} the integrated absorbance of per alkyl CH_2 stretching bands including both asymmetric stretching centered at 2925 cm^{-1} and symmetric stretching at 2854 cm^{-1} (the integrated absorbance of per alkyl CH_2 stretching bands was calculated by dividing the fitted CH_2 peak area in Figure S1 with the number of CH_2 for each sample, 9 for UO, 10 for undecanol, and 11 for UO-grafted MaCE and anodized PSi). We assumed that the integrated absorption coefficients of per O–H stretching and per alkyl CH_2 stretching were respectively equal for all four samples in Figure 6. If we use r_a, r_b, r_c, and r_d to represent for UO, undecanol, UO-grafted MaCE PSi, and UO-grafted anodized PSi respectively, then they were calculated from fitting results as r_a = 7.98, r_b =7.88, r_c = 4.52, and r_d = 0.89 (see calculations in Figure S1). In theory, r_a equals r_b, while here r_a = 7.98 and r_b = 7.88, which are quite close to each other. The yields of the target product of Si–$(CH_2)_{11}$–OH (or hydrosilylation efficiency) were derived by r_c/r_a % or r_c/r_b % as 57% on MaCE PSi and by r_d/r_a % or r_d/r_b % as 11% on anodized PSi respectively. The relative errors were assessed to be within 10% for MaCE PSi and 50% for anodized PSi by three repeating experimental measurements.

The hydrosilylation preference on MaCE PSi was explained by the abundance distributions of Si*H*$_x$ species and Si*H*$_x$ configurations in Section 3.1, where the SiH_2 species was suggested to possess higher hydrosilylation efficiency. The estimation method used here is quite effective for MaCE PSi samples because the porous layer is isotropic, thus the molecular orientations have little influence on the infrared strength; however for anodized PSi, the vertical nanowires and nanopores [14] rendered some of the grafted UO molecules to lie in a horizontal position, which influenced stretching strengths of O–H, C–H and maybe –CH=CH_2, thus the anisotropic property of surface-bound species brought deviations for this estimation method. To summarize, the higher –OH concentration, the lower Si–O stretching band at around 1100 cm^{-1}, and the lower residue Si*H*$_x$ stretching bands at around 2110 cm^{-1} on MaCE PSi convince us that the Si*H*$_x$ species possess higher hydrosilylation efficiency on MaCE PSi than on anodized PSi.

3.4 Growth of polymer brushes for protein microarray

Finally, we gave an example for protein microarray fabrication with MaCE PSi in Scheme 1. While with anodized PSi we failed to fabricate a control biochip by following the same experimental protocol because of the degradation and loss of the porous layer in the step of converting hydroxyl groups to initiators, which was a relatively harsh reaction environment with a long incubation time over 12 h and the release of HBr during the incubation period. MaCE PSi provided a much more robust porous layer, which could endure water boiling [19]. The stepwise chemical conversions on non-patterned chips were monitored with FTIR in Figure 7. As shown in Scheme 1 and Figure 7: (1) UO was grafted on MaCE PSi and its infrared trace was provided in Figure 6(b). (2) The surface initiator for ATRP, 2-bromopropionyl bromide, was attached through acylation, and verified by the carbonyl stretching band at 1710 cm^{-1} in Figure 7(a). (3) Poly(tert-butyl acrylate) brushes were grown via ATRP from the surface initiator, and proved with the strong and sharp ester stretching at 1733 cm^{-1} in Figure 7(b). (4) PAA brushes were obtained by hydrolysis of poly(tert-butyl acrylate) with methyl sulfonic acid and testified in Figure 7c by the strong and relatively wide carboxylic acid stretching at 1717 cm^{-1}, and also supported by the disappearance of –CH_3 stretching bands, indicating the tert-butyl groups had been cleaved. (5) NHS ester was obtained via EDC/NHS activation and evidenced by the typical tripartite band at 1817, 1786 and 1738 cm^{-1} in Figure 7(d). (6) Nitrilotriacetic acid (NTA) termini were obtained by amidation of NHS ester with ANTA and supported with amide bands at 1655 and 1565 cm^{-1} in Figure 7(e). The broad band feature around 1655 cm^{-1} is contributed partly from amide groups (amide I, C=O stretching) and also likely from oxidized surface species. The peak at around 1565 cm^{-1} is readily assigned to amide II band (C–N stretching coupled to N–H bending). Normally the peak area ratio of amide I over amide II is around 1.5. But in our case, the band at ~1565 cm^{-1} is much larger than amide I. The enhancement effect is caused mainly by the three acetates

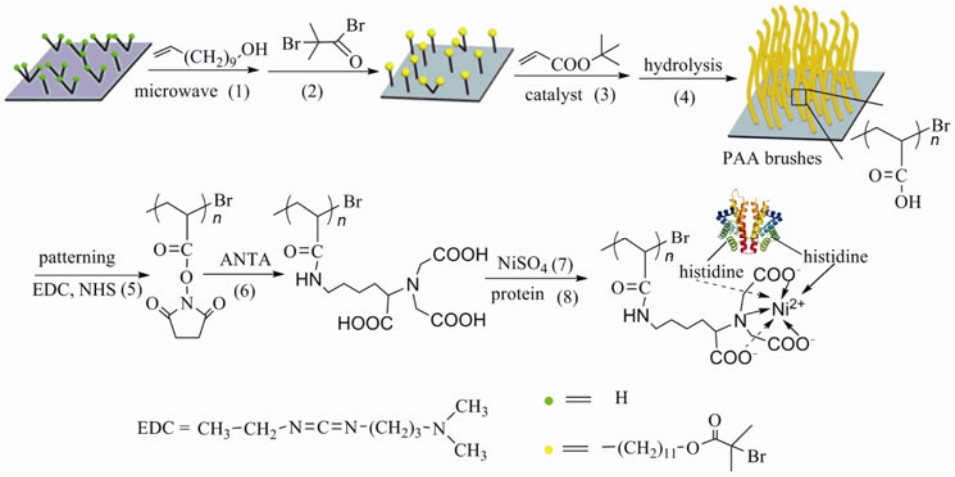

Scheme 1 Schematic chemistry route on MaCE PSi to immobilize FITC-labeled His-tagged protein [15, 16, 18, 19]. (1) ω-Undecenyl alcohol was grafted on PSi under microwave irradiation by surface hydrosilylation. (2) The end hydroxyl group was converted to a surface-bound initiator of 2-bromoisobutyryl group by acylation. (3) Poly(tert-butyl acrylate) brushes were grown via surface-initiated ATRP. (4) PAA brushes were obtained by post-treatment of hydrolysis [18]. (5) Patterning through photolithography and the exposed PAA patterns were activated by EDC/NHS to NHS ester side chains. (6) Adding ANTA, NHS ester was converted to NTA. (7) Ni^{2+} was loaded by adding $NiSO_4$. (8) Protein microarray was demonstrated by affinity binding of histidine-tagged proteins.

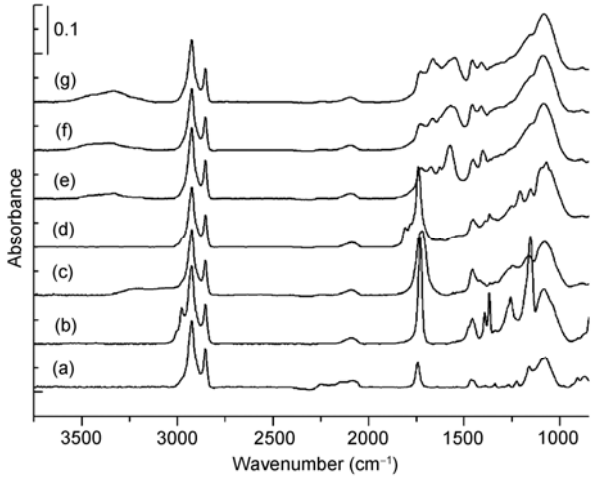

Figure 7 Transmission FTIR spectra of surface products through *in-situ* stepwise reactions: (a) surface-bound initiator of 2-bromoisobutyryl group; (b) poly(tert-butyl acrylate) brushes; (c) PAA brushes via acidification of poly(tert-butyl acrylate); (d) NHS ester via EDC/NHS activation; (e) NTA after addition of ANTA; (f) Ni^{2+} loaded; (g) histidine-tagged protein via affinity binding.

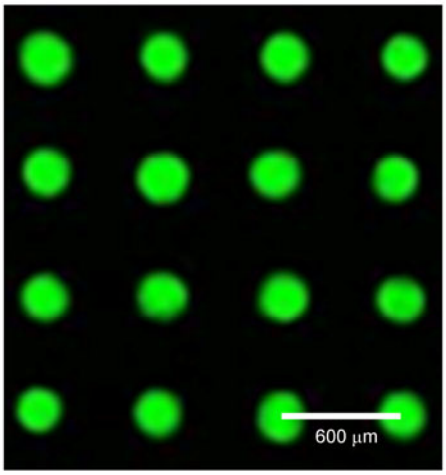

Figure 8 Fluorescence image of FITC-labeled His-tagged Trx-urodilatin microarray. The diameter of the spot is 200 μm and the neighbor spot-spot distance is 600 μm.

(COO^-) of NTA and partly by the hydrolysis of up to 30% NHS esters to quite a few carboxylate species, since the stretching band of carboxylate species is located at 1560 cm^{-1}. The band at 1730 cm^{-1} is assigned to the asymmetric stretching of organic esters already existed in the 2-bromoisobutyryl initiator for growing PAA brushes. (7) Ni^{2+} ions were loaded and (8) FITC-labeled His-tagged Trx-urodilatin was captured by affinity binding. Coordination of Ni^{2+} did not significantly change the infrared spectral trace in Figure 7(f) from 7(e). While after the protein was bound, Figure 7(g) presented obvious enhancement at 1655 cm^{-1}, due to the large amounts of protein amide groups.

A fluorescence microarray image was presented in Figure 8. We employed photolithography to fabricate microarrays on the PAA brushes covered PSi chip. After the microarray patterns were developed and PAA brushes exposed in patterns, the EDC/NHS treatment, ANTA amidation, and Ni^{2+} loading were carried out only in the pattern areas. Then the remaining photoresists were washed away with acetone. Finally the protein of FITC-labeled His-tagged Trx-urodilatin was captured by the well known NTA-Ni^{2+} histidine affinity binding. Figure 8 clearly shows the specific binding of FITC-labeled proteins to the NTA-Ni^{2+} functionalized patterns, while the PAA surroundings exhibit a quite low fluorescent background. According to a standard curve

we reported previously [16], the surface density of FITC-labeled His-tagged Trx-urodilatin was estimated as ~90 pmol/cm^2 (~7×10^4 counts), 4 times higher than in a monolayer mode, which was reasonable regarding the high payload capability of PAA brushes and the crowding effect of immobilized proteins. In addition the background PAA brushes were resistant to nonspecific adsorption of proteins [41]. Moreover combination of the stable porous structures of MaCE PSi and covalently grafted polymer brushes enhances the long-term chemical and mechanical durability of biochips in harsh environments over weeks and even months.

4 Conclusions

To summarize, instead of using the vulnerable anodized PSi under ambient conditions, we worked on the robust MaCE PSi for organic and biochemical modification, and further for fabrication of biochips. A specific advantage of MaCE PSi rather than anodized PSi for organic functionalization is its higher hydrosilylation efficiency, which is proposed to be caused by: (1) the higher SiH_2 component (53%) possessing high hydrosilylation reactivity and the lower SiH_1 and SiH_3 abundances attenuating side reactions, (2) the different silicon hydride configurations, hinted from ~6 cm^{-1} blue shift in the Si*H*x stretching bands from anodized PSi, possibly playing a role. In an etchant of 2:2:1 (*v*:*v*:*v*) HF(40%):H_2O_2(30%):EtOH, we optimized the thickness of Pt-coatings at 7–15 nm and the etching time at 3-10 min, regarding the quality of porous membrane, quantity of Si*H*x species, and cost. Deposition of a Pt film on silicon after removing the passivation silica layer greatly enhanced the Si*H*x quantity in the MaCE system. SEM imaging revealed that an isotropic meso-porous layer of hundreds of nanometers thick was the main supporting structure for organic functionalization. An example reaction with UO was shown to demonstrate the higher hydrosilylation efficiency of MaCE PSi by analyzing the integrated absorbance ratio of O–H stretching against per alkyl –CH_2 stretching. We derived a hydrosilylation efficiency of 57% for UO-grafting on MaCE PSi, while only 11% on anodized PSi. To end, we demonstrated a durable protein microarray using MaCE PSi as the supporting substrate. Combining surface chemistry and micro-fabrication technology, we grew PAA brushes, patterned the chip via photolithography, activated side carboxylic acids of PAA to NHS esters, prepared NTA-Ni^{2+} patterns via amination and coordination, and finally demonstrated histidine-tagged protein microarrays with fluorescence scanning. Silicon as substrate for biochip applications presents a prosperous future, due to the unique properties of this materials: large surface area-to-volume ratio, high density of binding sites, long-term durability in ambient conditions, easy integration with the micro-fabrication technology in semiconductor industry, and the multiple read-out mechanisms on silicon materials.

Suggestions and comments from anonymous reviewers are greatly appreciated. We thank the financial support of the National Basic Research Program of China (2013CB922101) and the National Natural Science Foundation of China (20827001, 91027019, 21021062).

1 Canham LT. Silicon quantum wire array fabrication by electrochemical and chemical dissolution of wafers. *Appl Ph Lett,* 1990, 57, 1046–1048
2 Canham LT, Cullis AG, Pickering G, Dosser OD. Luminescent anodized silicon aerocrystal networks prepared by supercritical drying. *Nature*, 1994, 368: 133–135
3 Lin VS, Motesharei K, Dancil KPS, Sailor MJ, Ghadiri MR. A porous silicon-based optical interferometric biosensor. *Science*, 1997, 278, 5339: 840–843
4 Sailor MJ. *Porous Silicon in Practice: Preparation, Characterization, and Applications*. Weinheim: Wiley-VCH, 2012
5 Menna P, Di Francia G, Laferrara V. Porous silicon in solar-cells–a review and a description of its application as an AR coating. *Sol Ener Mater Sol Cells*, 1995, 37: 13–24
6 Buriak JM. Organometallic chemistry on silicon and germanium surfaces. *Chem Rev*, 2002, 102: 1271–1308
7 Linford MR, Chidsey CED. Alkyl monolayers covalently bonded to silicon surfaces. *J Am Chem Soc*, 1993, 115: 12631–12632
8 Lees IN, Lin H, Canaria CA, Gurtner C, Sailor MJ, Miskelly GM. Chemical stability of porous silicon surfaces electrochemically modified with functional alkyl species. *Langmuir*, 2003, 19: 9812–9817
9 Xia B, Xiao SJ, Wang J, Guo DJ. Stability improvement of porous silicon surface structures by grafting polydimethylsiloxane polymer monolayers. *Thin Solid Films*, 2005, 474: 306–309
10 Han HM, Li HF, Xiao SJ. Improvement of the durability of porous silicon through functionalisation for biomedical applications. *Thin Solid Films*, 2011, 519: 3325–3333
11 Li X, Bohn PW. Metal-assisted chemical etching in HF/H_2O_2 produces porous silicon. *Appl Phys Lett*, 2000,77: 2572–2574
12 Chattopadhyay S, Bohn PW. Surfactant-induced modulation of light emission in porous silicon produced by metal-assisted electroless etching. *Anal Chem*, 2006, 78: 6058–6064
13 Douani R, Si-Larbi K, Hadjersi T, Megouda N, Manseri A. Silver-assisted electroless etching mechanism of silicon. *Phys Stat Sol (a)*, 2008, 205: 225–230
14 Guo DJ, Xiao SJ, Xia B, Wei S, Pei J, Pan Y, You XZ, Gu ZZ, Lu Z. Reaction of porous silicon with both end-functionalized organic compounds bearing α-bromo and ω-carboxy groups for immobilization of biomolecules. *J Phy Chem B*, 2005, 109: 20620–20628
15 Chen L, Chen ZT, Wang J, Xiao SJ, Lu ZH, Gu ZZ, Kang L, Chen J, Wu PH, Tang YC, Liu JN. Gel-pad microarrays templated by patterned porous silicon for dual-mode detection of proteins. *Lab Chip*, 2009, 9: 756–760
16 Jia P, Tang YC, Xu N, Lu W, Xiao SJ, Liu JN. Covalently derivatized NTA microarrays on porous silicon for multi-mode detection of His-tagged proteins. *Sci China Chem*, 2011, 54: 526–535
17 Li HF, Han HM, Wu YG, Xiao SJ. Biological functionalization and patterning of porous silicon prepared by Pt-assisted chemical etching. *Appl Surf Sci*, 2010, 256: 4048–4051
18 Wang C, Yan Q, Liu HB, Zhou XH, Xiao SJ. Different EDC/NHS activation mechanisms between PAA and PMAA brushes and the following amidation reactions. *Langmuir*, 2011, 27: 12058–12068
19 Wang C, Jia XM, Jiang C, Zhuang GN, Yan Q, Xiao SJ. DNA microarray fabricated on poly(acrylic acid) brushes-coated porous silicon by in-situ rolling circle amplification. *Analyst*, 2012, 137: 4539–4545
20 Wang C, Zhou XH, Han HM, Xiao SJ. Optimization of metal-assisted etchant components for fabrication of porous silicon. *Chin J Inorg Chem*, 2011, 12: 2332–2338

21 Linford MR, Fenter P, Eisenberger PM, Chidsey CED. Alkyl monolayers on silicon prepared from 1-alkenes and hydrogen-terminated silicon. *J Am Chem Soc*, 1995, 117: 3145–3155

22 Effenberger F, Götz G, Bidlingmaier B, Wezstein M. Photoactivated preparation and patterning of self-assembled monolayers with 1-alkenes and aldehydes on silicon hydride surfaces. *Angew Chem Int Ed*, 1998, 37: 2462–2464

23 Lee EJ, Bitner TW, Ha JS, Shane MJ, Sailor MJ. Light-induced reactions of porous and single-crystal Si surfaces with carboxylic acids. *J Am Chem Soc*, 1996, 118: 5375–5382

24 Warntjes M, Vieillard C, Ozanam F, Chazalviel JN. Electrochemical methoxylation of porous silicon surface. *J Electrochem Soc*, 1995, 142: 4138–4142

25 Boukherroub R, Morin S, Sharpe P, Wayner DDM. Insights into the formation mechanisms of Si–OR monolayers from the thermal reactions of alcohols and aldehydes with Si(111)–H[1]. *Langmuir*, 2000, 16: 7429–7434

26 Asanuma H, Lopinski GP, Yu HZ. Kinetic control of the photochemical reactivity of hydrogen-terminated silicon with bifunctional molecules. *Langmuir*, 2005, 21: 5013–5018

27 Buriak JM, Allen MJ. Lewis acid mediated functionalization of porous silicon with substituted alkenes and alkynes. *J Am Chem Soc*, 1998, 120: 1339–1340

28 Buriak JM, Stewart MP, Geders TW, Allen MJ, Choi HC, Smith J, Raftery D, Canham LT. Lewis acid mediated hydrosilylation on porous silicon surfaces. *J Am Chem Soc*,1999, 121: 11491–11502

29 Huck LA, Buriak JM. Toward a mechanistic understanding of exciton-mediated hydrosilylation on nanocrystalline silicon. *J Am Chem Soc*, 2012, 134: 489–497

30 Sieval AB, Linke R, Zuilhof H, Sudhölter EJR. High-quality alkyl monolayers on silicon surfaces. *Adv Mater*, 2000, 12: 1457–1460

31 Sun QY, de Smet LCPM, van Lagen B, Wright A, Zuilhof H, Sudholter EJR. Covalently attached monolayers on hydrogen-terminated Si(100): extremely mild attachment by visible light. *Angew Chem Int Ed*, 2004, 43: 1352–1355

32 Qin GT, Santos CM, Zhang W, Li Y, Kumar A, Erasquin UJ, Liu K, Muradov P, Trautner BW, Cai CZ. Biofunctionalization on alkylated silicon substrate surfaces via “click” chemistry. *J Am Chem Soc*, 2010, 132: 16432–16441

33 Michalak DJ, Amy SR, Aureau D, Dai M, Estève A, Chabel Y. Nanopatterning Si(111) surfaces as a selective surface-chemistry route. *Nat Mater*, 2010, 9: 266–271

34 Fidélis A, Ozanam F, Chazalviel JN. Fully methylated, atomically flat (111) silicon surface. *Surf Sci*, 2000, 444: L7–10

35 Li Y, Calder S, Yaffe O, Cahen D, Haick H, Kronik L, Zuilhof H. Hybrids of organic molecules and flat, oxide-free silicon: high-density monolayers, electronic properties, and functionalization. *Langmuir*, 2012, 28: 9920–9929

36 Huck LA, Buriak JM. Toward a mechanistic understanding of exciton-mediated hydrosilylation on nanocrystalline silicon. *J Am Chem Soc*, 2012, 134: 489–497

37 Zhong YL, Bernasek SL. Direct photochemical functionalization of Si(111) with undecenol. *Langmuir*, 2011, 27: 1796–1802

38 Brodsky MH, Cardona M, Cuomo JJ. Infrared and Raman spectra of the silicon-hydrogen bonds in amorphous silicon prepared by glow discharge and sputtering. *Phys Rev B*, 1977, 16: 3556–3571

39 Chabal YJ, Higashi GS, Raghavachari K, Burrows VA. Infrared spectroscopy of Si(111) and Si(100) surfaces after HF treatment: Hydrogen termination and surface morphology. *J Vac Sci Technol A*, 1989, 7: 2104–2109

40 Perrine KA, Teplyakov AV. Reactivity of selectively terminated single crystal silicon surfaces. *Chem Soc Rev*, 2010, 39: 3256–7324

41 Czeslik C, Jackler G, Hazlett T, Gratton E, Steitz R, Wittemann A, Ballauff M. Salt-induced protein resistance of polyelectrolyte brushes studied using fluorescence correlation spectroscopy and neutron reflectometry. *Phys Chem Chem Phys*, 2004, 6: 5557–5563

SCIENCE CHINA
Chemistry

• SUPPORTING INFORMATION •

August 2013 Vol.56 No.8: 1
doi: 10.1007/s11426-013-4849-1

High hydrosilylation efficiency of porous silicon SiH*x* species produced by Pt-assisted chemical etching for biochip fabrication

XIAO MinYu[1], HAN HuanMei[1,2] & XIAO ShouJun[1*]

[1]*State Key Laboratory of Coordination Chemistry, School of Chemistry and Chemical Engineering, Nanjing National Laboratory of Microstructures, Nanjing University, Nanjing 210093, China*
[2]*Jinan Entry-Exit Inspection and Quarantine Bureau Inspection, Jinan 250014, China*

Received December 22, 2012; accepted January 30, 2013; published online February 22, 2013

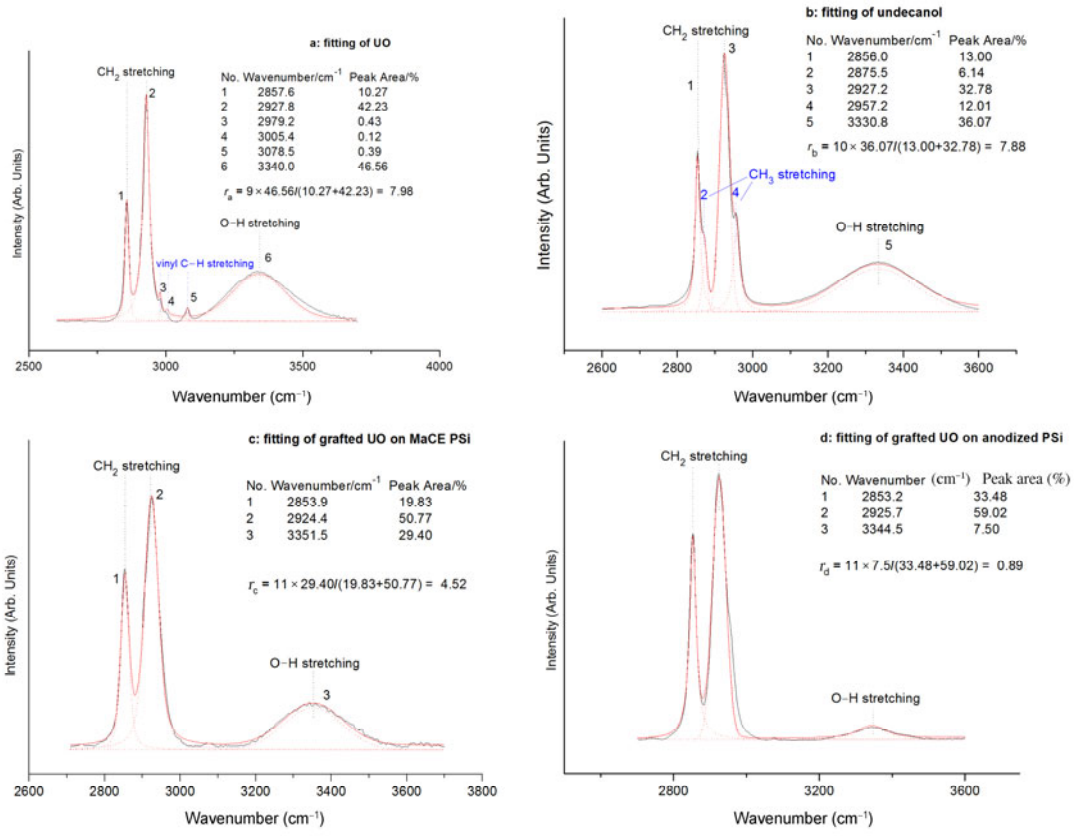

Figure S1 Fitting of the C–H and O–H stretching bands in the region from 2700 to 3700 cm^{-1}. Each resolved peak was assigned and assessed with a peak area percentage. $r = A_{OHs}/A_{CH2s}$, where A_{OHs} represents the integrated absorbance of O–H stretching band centered at 3340 cm^{-1}, and A_{CH_2s} the integrated absorbance of per alkyl CH_2 stretching bands including both asymmetric stretching centered at 2925 cm^{-1} and symmetric stretching at 2854 cm^{-1}. The integrated absorbance of per alkyl CH_2 stretching bands were calculated by dividing the fitted CH_2 peak area with the number of CH_2 for each sample (9 for UO, 10 for undecanol, and 11 for UO-grafted MaCE and anodized PSi). r_a, r_b, r_c, and r_d, representing UO, undecanol, UO-grafted MaCE PSi, and UO-grafted anodized PSi respectively, were calculated from fitting results as $r_a = 7.98$, $r_b = 7.88$, $r_c = 4.52$, and $r_d = 0.89$.

*Corresponding author (email: sjxiao@nju.edu.cn)